



City Research Online

## City, University of London Institutional Repository

---

**Citation:** Martinez, D., Morar, N., Khotari, M. & Gray, S. (2020). Investigation into the Effects of Salt Chemistry and SO<sub>2</sub> on the Crack Initiation of CMSX-4 in Static Loading Conditions. *Superalloys 2020*, pp. 753-762. doi: 10.1007/978-3-030-51834-9\_73 ISSN 2367-1181 doi: 10.1007/978-3-030-51834-9\_73

This is the accepted version of the paper.

This version of the publication may differ from the final published version.

---

**Permanent repository link:** <https://openaccess.city.ac.uk/id/eprint/30210/>

**Link to published version:** [https://doi.org/10.1007/978-3-030-51834-9\\_73](https://doi.org/10.1007/978-3-030-51834-9_73)

**Copyright:** City Research Online aims to make research outputs of City, University of London available to a wider audience. Copyright and Moral Rights remain with the author(s) and/or copyright holders. URLs from City Research Online may be freely distributed and linked to.

**Reuse:** Copies of full items can be used for personal research or study, educational, or not-for-profit purposes without prior permission or charge. Provided that the authors, title and full bibliographic details are credited, a hyperlink and/or URL is given for the original metadata page and the content is not changed in any way.

---

City Research Online:

<http://openaccess.city.ac.uk/>

[publications@city.ac.uk](mailto:publications@city.ac.uk)

---

# TMS Superalloys 2020

## Investigation into the effects of salt chemistry and SO<sub>2</sub> on the crack initiation of CMSX-4 in static-loading conditions

F. Duarte Martinez<sup>1</sup>, N.I. Morar<sup>1</sup>, M. Kothari<sup>1</sup>, G. Gibson<sup>2</sup>, J. Leggett<sup>2</sup>, J.C. Mason-Flucke<sup>2</sup>, J.R. Nicholls<sup>1</sup>, G.M. Castelluccio<sup>1</sup>, S. Gray<sup>1</sup>

<sup>1</sup> SEPI, Cranfield University, Bedford, MK43 0AL, UK <sup>2</sup>Rolls-Royce plc, PO Box 31, Derby, DE24 8BJ, UK

**Keywords:** CMSX-4, C-ring, Hot Corrosion, X-ray Computed tomography, FactSage 7.3

### 1. Abstract

Although evidence exists of the potential impact of stress, co-incident with corrosive environments at high temperature, for single crystal turbine blades, the mechanism responsible is not fully understood. This work explores the effect of CaSO<sub>4</sub>, Na<sub>2</sub>SO<sub>4</sub> and sea salt on the scale formation and crack initiation of CMSX-4 at 550°C in 50 ppm of SO<sub>2</sub> and synthetic air under a static stress of 800 MPa. The cross-sectional analysis showed that the CaSO<sub>4</sub> and the Na<sub>2</sub>SO<sub>4</sub> salted specimens did not undergo a significant degree of corrosion degradation and no cracks were detected after 400 hours of exposure. However, sea salt caused significant degradation to the scale and cracks were detected by X-ray CT scanning after 400 hours of exposure. The findings from this study suggests that the sulfation of chlorine containing species in sea salt led to the formation, vaporisation and re-oxidation of metal chlorides and this mechanism was found to play a key role in the formation of a non-protective scale. An active oxidation mechanism has been proposed to interpret the results. In conclusion, it is hypothesized that due to the synergistic effect of stress and the formation of a non-protective scale, fast diffusion paths for sulfur, oxygen and chlorine ingress were formed. Further work is currently being undertaken to understand the effect of these species on the local embrittlement of CMSX-4 that ultimately led to the initiation of cracks in the specimen.

### 2. Introduction

The aviation industry has continued to increase the efficiency of gas turbine engines, which are now designed to operate a wide variety of flight routes. In general, the efficiency drive has led to components spending longer times at temperatures above which corrosion mechanisms can occur. This has led to a complex degradation mechanism being identified in the region under the platform of single crystal turbine blades. In these regions of the blade, the synergistic effect of stress and high temperature aggressive environments plays a crucial role in its structural integrity, hence a fundamental understanding of crack initiation mechanisms is the key to develop the next generation of high temperature materials and protection methods.

CMSX-4 is a third-generation single crystal nickel-based superalloy commonly used for turbine blades due to its high temperature creep strength. This property has been achieved by alloying with elements such as aluminium and titanium to increase the volume fraction of  $\gamma'$ , whilst reducing the level of chromium. The reduction of chromium in turbine blade alloys has meant that such alloys are not immune to attack from type I or type II hot corrosion, which leads to complex degradation mechanisms [1, 2].

Mechanisms of hot corrosion have been widely studied and can be categorised into high temperature hot corrosion (800-950°C) and low temperature hot corrosion (650-750°C) [3]. Low temperature hot corrosion depends significantly on the SO<sub>2</sub>/SO<sub>3</sub> ratio in the gas composition [4]. The partial pressure of SO<sub>3</sub> can influence the type of sulphate formation and affects the deposit's melting point. However, below 600°C the kinetics of hot corrosion reduces significantly due to the lack of conversion of SO<sub>2</sub> to SO<sub>3</sub> and consequently, research is ongoing into identifying new low temperature cracking mechanisms at these intermediate temperatures. Although the hot corrosion attack is typically considered to be associated with molten deposits of Na<sub>2</sub>SO<sub>4</sub>, a common mineral deposit present in the region under the platform of turbine blades is anhydrous calcium sulphate and it has been reported to be present in locations where unpredictable failures have occurred. Nevertheless, the effect of CaSO<sub>4</sub>

on the corrosion degradation and crack initiation mechanisms in stressed components has not yet been investigated at intermediate temperatures.

In addition, sea salt is a main contaminant in air and the reaction of alkali chlorides (contained in sea salt) with  $SO_2$  from the combustion of the fuel can produce  $Cl_2$  according to the following expression.



Although much work has been devoted to understanding the degradation mechanisms due to molten sulphates and sulfur-containing gases, the effect of  $Cl_2$  on the scale formation and crack initiation in single crystal superalloys, such as CMSX-4 is less well understood. Therefore, the study of its degradation mechanism in single crystal turbine blade materials under stress and at intermediate temperatures is highly relevant to understanding its mode of attack.

The aim of the present research is twofold. Firstly, to develop a methodology that enables to test the synergistic effect of stress and high temperature aggressive environments on the mechanisms of crack initiation in anisotropic materials. Secondly, to use the developed methodology to understand the effect of  $CaSO_4$ ,  $Na_2SO_4$  and sea salt on the scale formation and crack initiation of CMSX-4 at a high temperature and sulfur containing environment.

### 3. Experimental

#### 3.1 Stress corrosion test

We employ constant-strain C-ring stress corrosion (SC) tests with five steps and three sub-steps, as shown in Figure 1. The initial three steps follow ISO 7539-5 [5] and ASTM G38 [6] standard test methods. However, these test standards do not provide the guidelines for the salt deposition and environmental exposure (i.e., simulating the gas turbine environment). Hence, Cranfield's Surface Engineering Research Group has developed guidelines for the salt deposition and environmental test procedures, which were used for the C-ring stress corrosion tests.

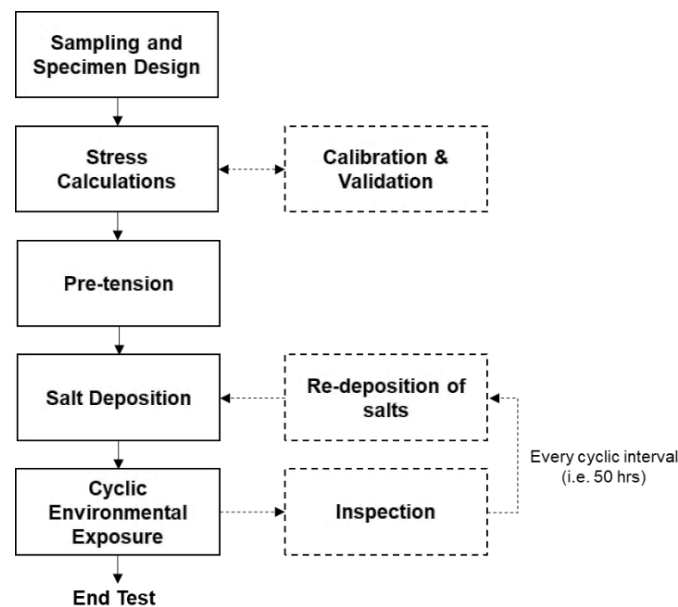


Figure 1. Test method flow chart of the C-ring stress corrosion test

#### 3.2 Material sampling and specimen design

The C-ring test specimens were produced from CMSX-4 bars in the fully solutioned and aged heat-treated condition as per Rolls Royce Plc. specification with a [001] crystallographic orientation aligned with the cylinder axis, following ISO 7539-5 guidelines. The composition of CMSX-4 is listed in Table 1. A total of nine C-ring specimens were prepared for the stress corrosion testing. As shown in Figure 2, two through holes of 7.0 mm ( $\pm 0.05$ ) diameter were drilled to compress the C-ring using a bolt, nut and two washers. The bolt, nut and washers used are made of commercial Waspalloy given its high temperature corrosion and creep resistance.

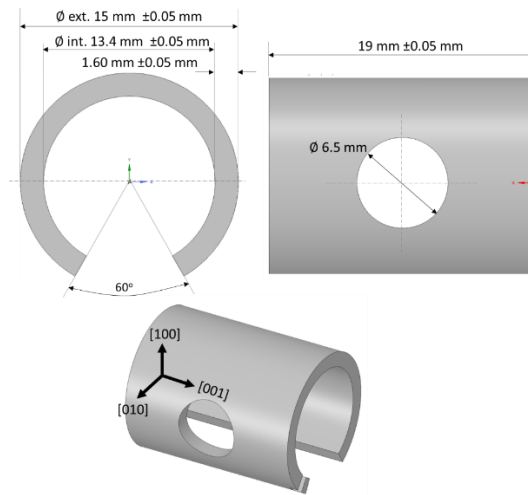


Figure 2. Dimensions of C-ring specimens

Table 1. Chemical composition of CMSX-4 (wt%)

Ni	Cr	Al	Co	Ta	W	Mo	Ti	Re	Hf
Bal.	6.5	5.6	9.0	6.5	6.0	0.6	1.0	3.0	0.1

### 3.3 Maximum stress estimation

According to the standard test guidelines, the required displacement to achieve a target stress level is calculated theoretically following the Equation 1 and 2 from ISO 7539-5. The constant-strain C-ring test involves constraining the specimen by tightening a bolt on one side and a nut on the other, such that the stress level in the apex region of the C-ring achieves the desired stress and does not exceed the material's yield strength at room temperature. However, the equations 1 and 2 from ISO 7539-5 are only valid for isotropic materials. Therefore, the stress calculation method that follows standards [5, 6] could not be used due to the anisotropic nature of the single crystal superalloy CMSX-4, also the fact that the standards does not account for any thermal expansion effects. For this reason, Finite Element (FE) modelling was used to compute the stress distribution at the C-ring apex region, where the local stress is found to be at peak. This method enables to consider not only the anisotropic nature of materials but also the thermal expansion effect; hence, increasing the accuracy in the predicted displacement required for a given target stress level.

A commercial FE software Ansys Workbench v19 was used to perform a static analysis of the C-ring model and compute the stress distribution. For simplicity, a three-dimensional (3-D) half geometric model of a C-ring assembly was used for the FE analysis (see Figure 3), and it follows the dimensions of the actual C-ring test specimen. Material properties, including the elastic constants and coefficient of thermal expansion, were provided by industrial collaborator (Rolls-Royce plc). A higher order 3-D solid 10 node element (SOLID187) and 20 node element (SOLID186) was considered and the contact of surface to surface friction (input value of 0.3). In accordance with actual test conditions, the loading is set in two steps, viz. pre-tension and then thermal load. First step, load by displacement to mimic the initial bolt-nut pre-tension procedure at room temperature (22°C). Axial displacement and nodal constraint were applied between the both bottom end face of the bolt and C-ring to cause a pre-determined amount of deflection in the tension mode, as shown in Figure 4.

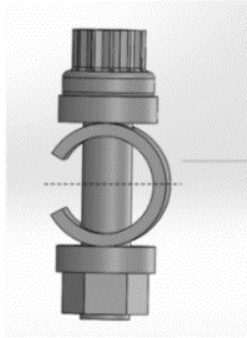


Figure 3 – Half geometric model of C-ring assembly

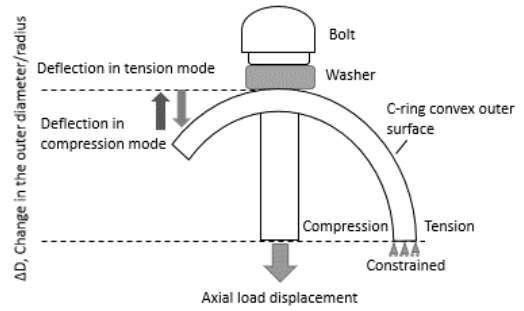


Figure 4 – Pre-tensioning of C-ring specimen

The second step was to apply the thermal condition to simulate the actual test temperature (550°C). In this step, thermal expansion occurs on the C-ring and the bolt, which causes a change of the deflection in compression mode. In terms of the solution, the Maximum Principal Stress (MPS) distribution criterion is read as the calculation results of the C-ring model, as shown in Figure 5 and Figure 6.

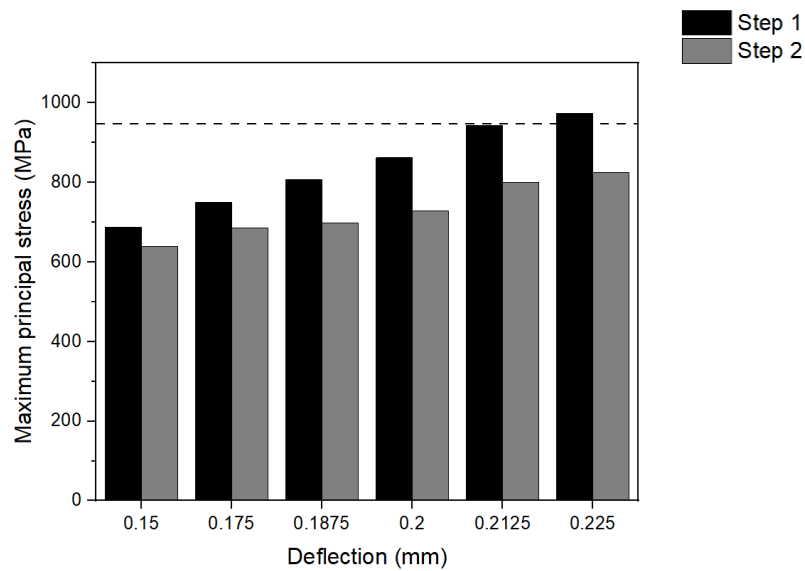


Figure 5. Maximum principal stress values at peak location at step 1 and step 2 conditions

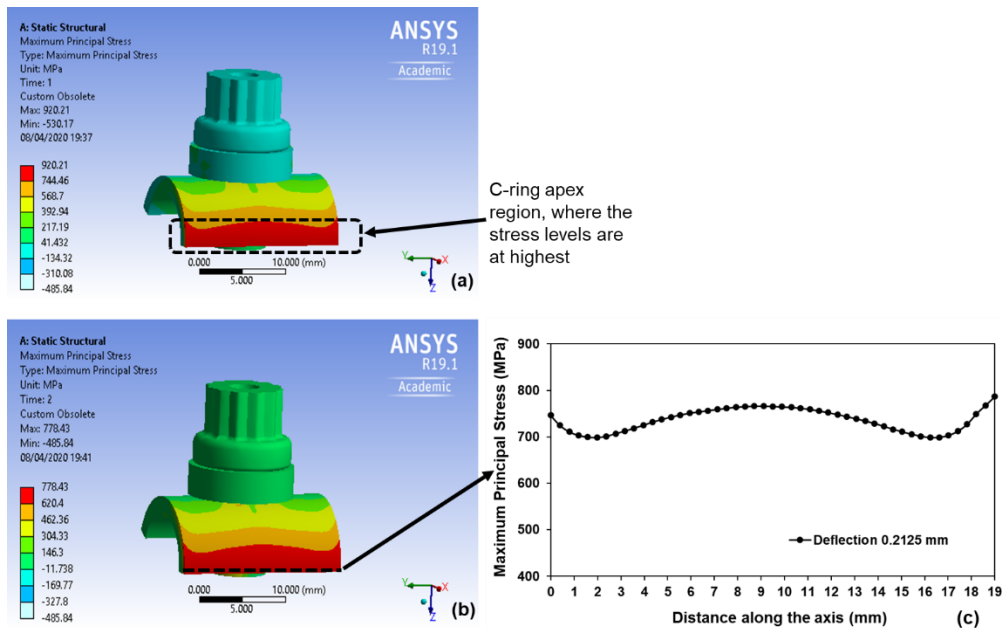


Figure 6. (a) Stress distribution in the C-ring in step 1 condition (22°C); (b) stress distribution in the C-ring in step 2 condition (550°C); (c) stress distribution at the mid apex region of the C-ring at (550°C)

Figure 5 shows the results of the FE simulations conducted at different load displacement values ranging from 0.15 mm to 0.225 mm on the half plane C-ring model. The MPS at the peak location drops as it increases to actual test temperature from 22°C (step 1) to 550°C (step 2) due to the thermal expansion, which changes the deflection in compression mode. The dotted line in Figure 5 outlines the yield strength of the C-ring material, suggesting that the required load displacement corresponding to C-ring material yield strength at 22°C is 0.2125 mm. Therefore, a pre-tension displacement of 0.425 mm was applied for all C-ring test specimens, corresponding to a stress level of 800 MPa with a nominal tolerance of  $\pm 25$  MPa at 550°C in the apex region. Figure 6 shows the MPS distribution of the half C-ring model under the defined test conditions.

To validate the FE simulation, the strain was measured by strain gauges mounted on 3 C-ring specimens at an angle of 90° from the vertical axis and applied OD deflection of 0.425 mm. The results yield a strain value at the gauge location of 0.0053, which agrees with 0.0056 – computed from FE and supports the correct estimation of stress applied to C-ring tests.

### 3.4 C-ring pre-tension

The actual C-ring test specimens are pre-tensioned to the determined amount of deflection of 0.425 mm with a tolerance of  $\pm 0.02$  mm. The procedure consists of tightening a bolt centred on the diameter of the C-ring using a torque wrench, which generates a tensile stress on the convex outer surface of the C-ring. The level of tensile stress is directly related to the degree of tightening of the bolt and amount of deflection produced, which is in turn associated to the reduction in the outer diameter (OD) of the C-ring. Measurements of the initial and final outer diameter were recorded at four different locations along the C-ring width using a digital micrometre to confirm the determined target deflection obtained. Under the pre-tension stage, the maximum principal stress at peak location is 920 MPa, which does not exceed the yield strength of CMSX-4 (939 MPa). Therefore, the integrity of the C-ring is considered adequate under the defined test conditions.

### 3.5 Salt deposition, exposure and characterisation

The C-ring specimens were cleaned in an ultrasonic bath with IPA (Isopropyl alcohol) before the exposure.  $\text{CaSO}_4$ ,  $\text{Na}_2\text{SO}_4$  and sea salt were applied, respectively, on each of the three specimens to be tested, with the deposit flux controlled according to the deposit recoat methodology [7] with a target deposition flux of 1.2  $\mu\text{g}/\text{cm}^2/\text{h}$ . The composition of sea salt is shown in Table 2.

Table 2. Chemical composition of sea salt (wt%)

NaCl	NaHCO <sub>3</sub>	KCl	NaBr	MgCl <sub>2</sub>	MgSO <sub>4</sub>	CaCl <sub>2</sub>
76.6	0.58	2.13	0.82	7.01	9.65	3.21

Following the deposition of the salt, the samples were exposed to a gaseous atmosphere containing air-50 ppm SO<sub>2</sub> in a controlled horizontal furnace. The specimens were removed from the furnace every 50 hours for crack detection using an optical microscope and non-destructive Eddie Current (EC). If no cracks were detected, the specimens were re-salted and exposed for a further 50 hours. After 400 hours of exposure, the three specimens with different salts deposits (CaSO<sub>4</sub>, Na<sub>2</sub>SO<sub>4</sub> and sea salt) were removed for X-ray CT scanning. The remaining of this paper focuses on the scale formation mechanisms in these three specimens.

The system used for XCT scanning was Nikon 225 KV. During the setup, the C-ring specimens were placed on a rotating table between the X-ray source and the detector, and were rotated about the central axis in the vertical direction. Further information regarding the XCT scanning parameters can be found in Table 3. After XCT examination, the samples were sectioned using oil lubricant and subsequently they were mounted in a 50:50 mixture of ballotoni and epoxy resin, ground and polished to a 1 μm diamond paste finish.

Table 3 - XCT scanning parameters used in this study

Parameter	Voxel size (μm)	Amperage (μA)	Magnification	Projections	Exposure time (ms)
Value	12.5	200	x16	3142	500

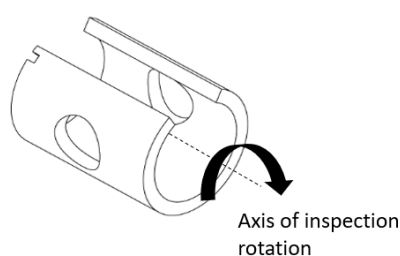


Figure 7. Rotation axis of the C-ring specimen during XCT scanning

### 3.6 Analytical methods

The cross-sectional analysis of the corroded specimens was undertaken with a Tescan Vega 3 at 20 KV scanning electron microscope (SEM) for imaging, and an Oxford Instruments energy dispersive x-rays (EDX) detector for qualitative chemical analysis.

## 4. Results

Table 4 summarizes the results obtained from the test. The results indicate that the CaSO<sub>4</sub> and the Na<sub>2</sub>SO<sub>4</sub> salted specimens did not initiate cracks, but severe cracking was detected in the specimen salted with sea salt. Figure 8 shows XCT images of the cracks in the specimen salted with sea salt.

Table 4. Summary of test results (EC\*: Eddie current)

Salt	Sample number	Test duration	Result
CaSO <sub>4</sub>	Sample 1	Tested for 400 hours	XCT scanned, no cracks present EC - no cracks present
	Sample 2	Tested for 500 hours	No XCT scan EC - no cracks present
	Sample 3	Tested for 500 hours	No XCT scan EC - no cracks present

Na <sub>2</sub> SO <sub>4</sub>	Sample 1	Tested for 400 hours	XCT scanned, no cracks present	EC - no cracks present
	Sample 2	Tested for 500 hours	No XCT scan	EC - no cracks present
	Sample 3	Tested for 500 hours	No XCT scan	EC - no cracks present
Sea salt	Sample 1	Tested for 400 hours	XCT scanned, cracks present	EC - cracks present
	Sample 2	Tested for 500 hours	No XCT scan	EC - cracks present
	Sample 3	Tested for 500 hours	No XCT scan	EC - cracks present

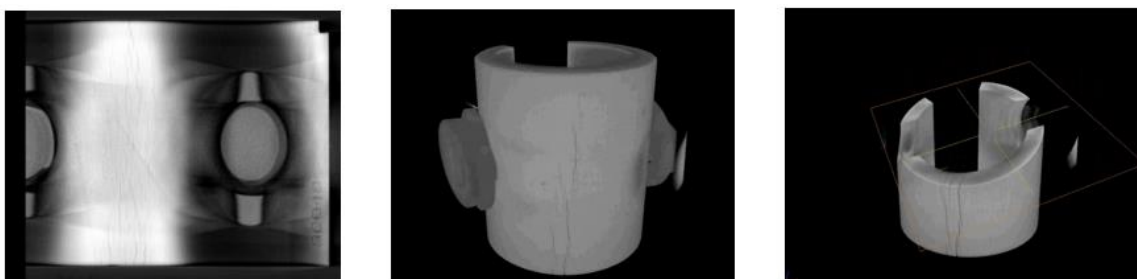


Figure 8. XCT scanning images of the specimen salted with sea salt

#### 4.1 Cross-sectional analysis

##### 4.1.1 Scale formation on the specimens salted with CaSO<sub>4</sub> and Na<sub>2</sub>SO<sub>4</sub>

Figure 9 shows back-scattered electron (BSE) cross sectional images of three regions within the apex of the C-ring for each of the salted specimens and energy dispersive x-rays (EDX) analysis was undertaken to support the experimental findings. The CaSO<sub>4</sub> and the Na<sub>2</sub>SO<sub>4</sub> salted specimens did not undergo a significant degree of corrosion degradation and cracks were not detected after 400 hours of exposure. The elemental distribution maps of the Na<sub>2</sub>SO<sub>4</sub> and CaSO<sub>4</sub> salted specimens suggest the formation of a thin and dense layer rich in aluminium and chromium in the innermost part of the scales. On both specimens, the salts seem to be unreactive with the scale or base alloy and the enhanced local attack of the base alloy was not observed. No internal attack was observed on the CaSO<sub>4</sub> salted specimen. For the Na<sub>2</sub>SO<sub>4</sub> coated specimen there appears to be preferential attack of the  $\gamma$  phase below the surface of the Na<sub>2</sub>SO<sub>4</sub> salted specimen to a depth up to 5  $\mu\text{m}$ . This may have had a detrimental effect on the mechanical properties of the sub surface of the specimen, but not to a sufficient extent to initiate cracks.

##### 4.1.2 Scale formation on the specimen salted with artificial standard sea salt

The scale formed on the specimen salted with sea salt showed a higher degree of corrosion degradation than the other two specimens. The scales formed were highly porous, less adherent to the alloy and showed a higher tendency to spall during cooling compared to the other two specimens. Penetration of corrosion products seems to suggest the preferential attack of the  $\gamma'$  and the initiation of cracks was observed across the sample. Chlorine, one of the aggressive corrosive species present in sea salt, was detected at the alloy/scale interface as shown in Figure 10. Figure 11 shows a region of internal attack rich in aluminium, oxygen, chlorine and traces of sulfur that extends approximately 1  $\mu\text{m}$  into the base alloy. Although this behaviour was only observed in certain regions of the specimen, it provides evidence that chlorine can penetrate the scale and diffuse into the substrate. The implications of this will be discussed in a later section.

Figure 11 shows a nickel and chromium depletion layer within the alloy, just below the alloy's surface, and a porous layer of nickel oxide and chromium oxide in the outermost region of the scale. A thin titanium rich layer was formed adjacent to the alloy surface. EDS maps of other regions of the specimen salted with sea salt have

also been examined (not included in this paper). These EDS maps showed, as highlighted in Figure 9 (g), oxide scales rich in Al and Cr of approximately 2-3  $\mu\text{m}$  thickness in the innermost part of the scale, and regions rich in NiO in the outermost part of the scale. Although oxide scales rich in Al and Cr were also detected in the specimens salted with  $\text{CaSO}_4$  and  $\text{Na}_2\text{SO}_4$ , these scales were typically less than 1  $\mu\text{m}$  thick. Also, no Ni or Ti rich scales were observed in these two sulphate coated specimens; perhaps they were present, but in minor quantities below the detection limits. Given the presence of chlorine at the alloy/scale interface, this accelerated oxidation of alloy elements in the specimen salted with sea salt may have potentially occurred due to the oxidation of metal chlorides as will be discussed in a later section. The fact that no  $\text{NiCl}_2$  or  $\text{CrCl}_2/\text{CrCl}_3$  was detected at the alloy/scale interface was possibly due to its low concentration and the detectability limit of the EDS mapping. However, further work is in progress to validate this chloride-based corrosion/cracking mechanism.

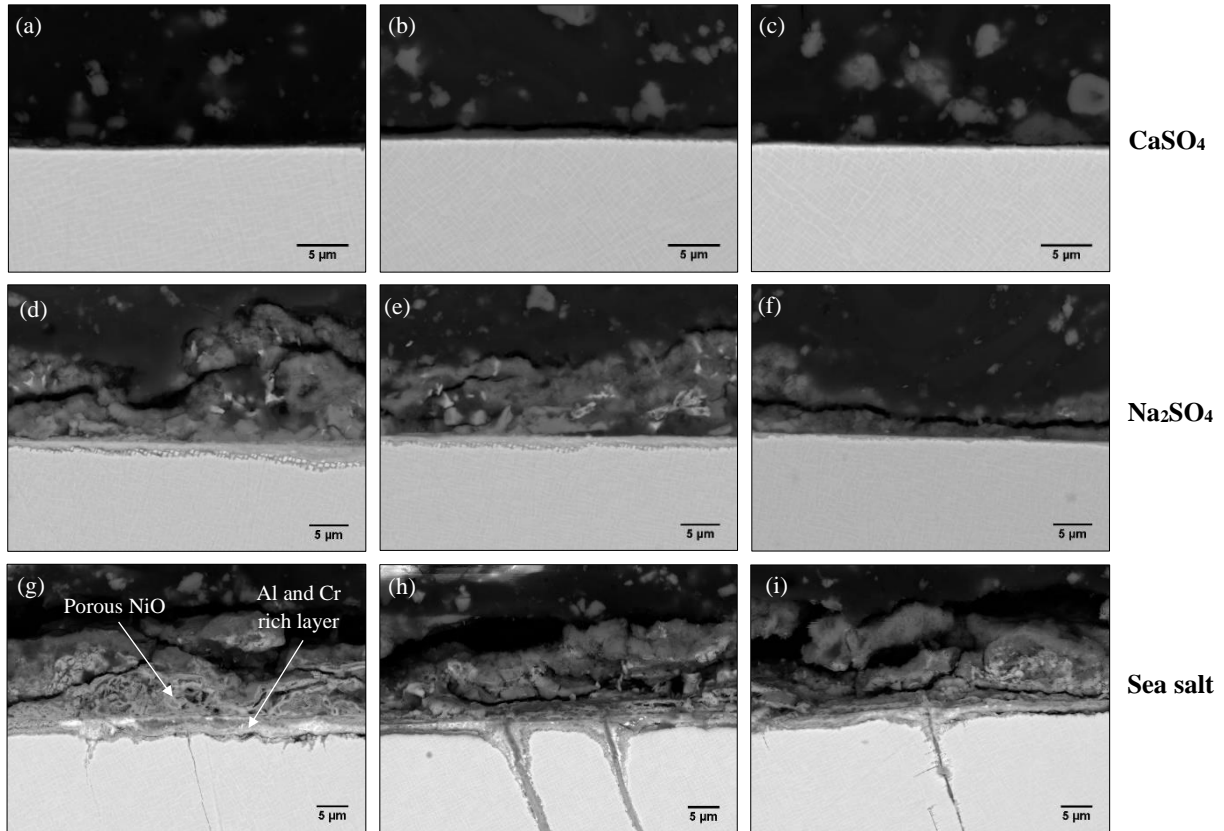


Figure 9. Backscattered electron cross-sectional images of the specimens salted with (a), (b) and (c)  $\text{CaSO}_4$ ; (d), (e) and (f)  $\text{Na}_2\text{SO}_4$ ; (g), (h) and (i) sea salt

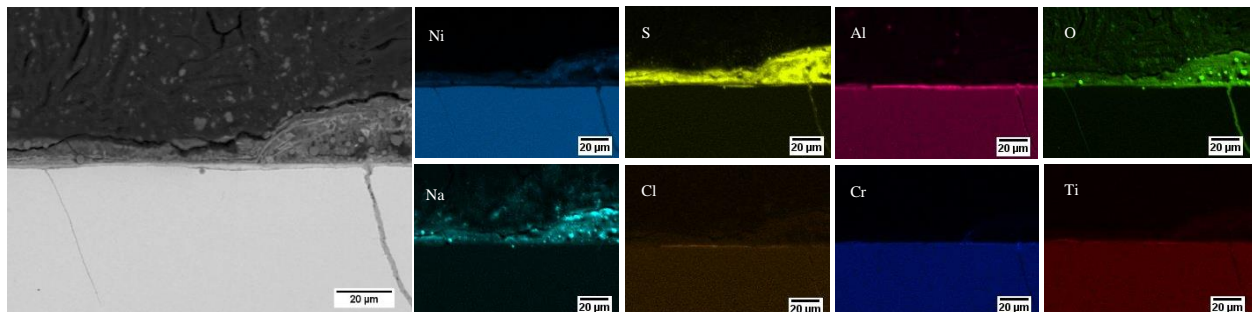


Figure 10. EDS mapping of a region within the apex of the specimen salted with sea salt

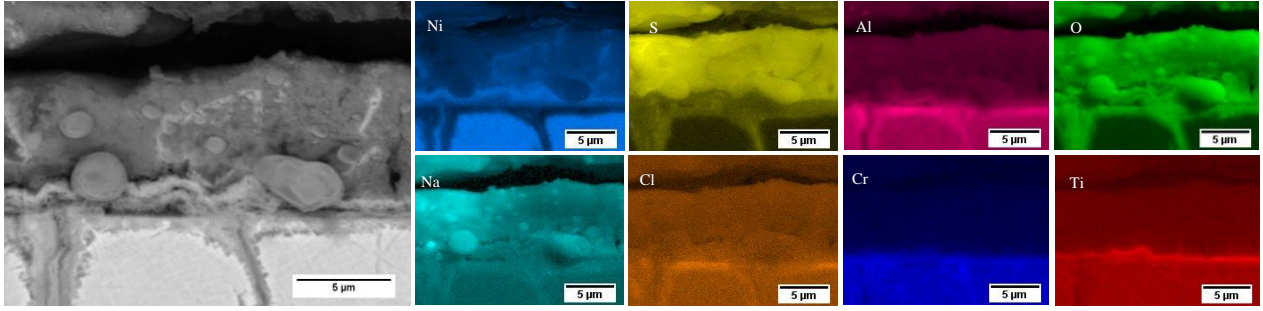


Figure 11. EDS mapping of an additional region within the apex of the specimen salted with sea salt

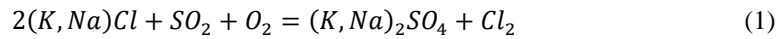
The elemental distribution map (Figure 11) showed regions of  $\text{Na}_2\text{SO}_4$  in the outer region of the scale. It is suggested that the formation of gaseous chlorine due to the sulphation of  $\text{NaCl}$  and perhaps other alkali chlorides had occurred in the sea salt coated specimen and this had significant implications in the degradation of the scale.

Ultimately, the combination of a porous scale, the poor adherence at the scale/alloy interface and consequently, the non-protective nature of the scale formed in the specimen salted with sea salt are critical factors that potentially led to the inward transport of corrosive and embrittling species, that caused the initiation of cracks in the specimen. The corrosion mechanism, defined as “active oxidation” as described by Grabke et al. [8, 9], was adopted to interpret the results regarding the formation of a non-protective scale. This mechanism consists of the formation, diffusion and re-oxidation of metal chlorides as will be further discussed in this paper.

## 5. Discussion

The experimental results in this study show that the high temperature degradation of CMSX-4 is greatly accelerated by the presence of sea salt. It is suggested that chlorine plays an important role in enhancing the oxidation of alloying elements, while making the oxide scale porous and loose. Based on the experimental findings, some thermodynamic considerations are provided in this section as a basis for interpreting the observed results.

Firstly, the presence of  $\text{SO}_2$  caused the sulphation of sodium chloride to sodium sulphate, which released chlorine at the scale/gas interface according to the following expression.



Some of the chlorine liberated will be lost to the environment; however, a small fraction can diffuse through the scale to the alloy/scale interface. In this region, there is a low partial pressure of  $\text{O}_2$ , hence chlorine will react with metal elements to form metal chlorides as described in the expression below.



From thermodynamic analysis, predominance diagrams of oxygen-chlorine-metal systems have been constructed for chromium, nickel and aluminium assuming unit activity of the metals (calculated using FactSage 7.3). Predominance diagrams are useful as they enable us to predict the phases that may be present as a function of  $P_{\text{O}_2}$  and  $P_{\text{Cl}_2}$ . If chlorine diffused through the scale and reached regions of low  $P_{\text{O}_2}$  (Figure 12), the formation of stable  $\text{Al}_2\text{Cl}_6$ ,  $\text{NiCl}_2$  and  $\text{CrCl}_2$  and/or  $\text{CrCl}_3$  would be thermodynamically possible. Furthermore, the driving forces ( $\Delta G$ ) for the formation of the metal chlorides shown below suggest that aluminium may be preferentially attacked or that a less reactive behaviour is expected for chromium and nickel chloride than aluminium chloride.



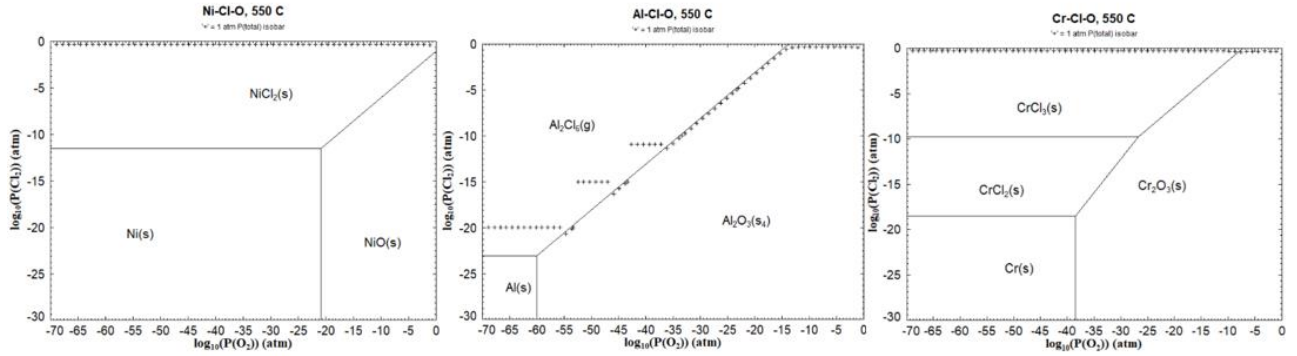
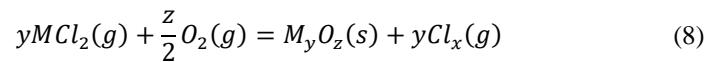


Figure 32 - Predominance diagrams of metal-oxygen-chlorine systems

The metal chlorides formed are highly volatile, therefore, they diffuse outwards through cracks and pores in the scale towards the gas/scale interface under the driving force of favourable gradients in vapour pressure [10, 11]. Within the scale, the partial pressure of oxygen increases, hence the gaseous chlorides will form solid oxides upon reaching higher oxygen partial pressures as shown in the reaction below.



The morphology of the oxides formed from the oxidation of metal chlorides tends to form nano-scale individual particles [12], hence the scales that formed during the test tend to be non-continuous and porous, yielding them a non-protective scale. It is suggested that this formation of a non-protective scale is what drives the diffusion of corrosive species through the scale, causing enhanced attack of the base alloy.

Given the oxygen gradient through the oxide scale, various metal chlorides will oxidise at different distances from the alloy surface. This  $P_{O_2}$  in which metal chlorides oxidise is predictable using the predominance diagrams in Figure 12. For instance, the predominance diagram suggests that  $NiCl_2$  would oxidise at higher  $P_{O_2}$  compared to  $Al_2Cl_6$  and  $CrCl_2/CrCl_3$ . Therefore, we should expect  $Al_2Cl_6$  and  $CrCl_2$  to oxidise closer to the metal surface compared to  $NiCl_2$ , which is in good agreement with the experimentally observed results.

Ultimately, the oxidation of metal chlorides releases chlorine, which can re-enter the corrosion process and repeat the active oxidation mechanism leading to a continuous loss of metal. Hence, chlorine acts as a catalyst, which may explain the accelerated oxidation observed in the specimen salted with sea salt. As can be inferred, the corrosion behaviour of alloys in chlorine containing environments is largely determined by the free energy of chloride formation, the vapour pressure of the metal chlorides and the oxygen partial pressure required to oxidise the evaporated chloride to an oxide.

Another characteristic feature that is in good agreement with the active oxidation mechanism is the reduced adhesion of the alloy-scale interface observed. The poor adherence and the large thermal expansion mismatch between the scale and the alloy may have resulted in the severe spallation and oxide fracture during cooling. This is explained by Elliott and Marsh [13], suggesting that the presence of voids and chloride rich phases at the oxide-alloy interface can have the combined effect of reducing the total contact area between the alloy and the scale, and eventually this may have contributed significantly to the spallation of the scale observed in this test. The poor adherence is further enhanced due to the growth stresses that arise near the alloy/scale interface as a result of the oxidation of metal chlorides, which may also lead to further cracking of the scale [10, 14, 15].

Given the ingress of other species through the scale, the poor adherence may also be associated with an interfacial segregation of sulfur and can result in a partial detachment of the scale from the metal substrate. This harmful effect of sulfur has been known to weaken the bonding of the alloy/oxide interface rendering the resulting scale non-adherent [16, 17]. Ultimately, the presence of chlorides at the scale/alloy interface as well as the segregation of sulfur are probably important causes that leads to the low adherence of the scale/alloy interface, and consequently the non-protective nature of the scale formed on the specimen.

## 6. Conclusions

In this study, the synergistic effect of stress and three salts (CaSO<sub>4</sub>, Na<sub>2</sub>SO<sub>4</sub> and sea salt) on the scale formation of CMSX-4 in a sulfur containing environment at 550°C was investigated. This study has demonstrated that the chlorine contained in sea salt causes significant damage to the scale formation on CMSX-4, potentially through an active oxidation mechanism. Sulfur played a contributory role to the corrosion process by permitting the release of chlorine.

The non-protective, non-adherent and discontinuous scale leads to the potential ingress of corrosive and embrittling species that interact with the base alloy and leads to the initiation of cracks. Ultimately, more in-depth analysis is required to confirm the active oxidation mechanism as proposed in this study. For instance, the mechanism of chlorine diffusion through the scale should be further investigated and the phases formed must be evaluated by means of characterisation techniques, such as x-ray photoelectron spectroscopy (XPS) or selective area diffraction pattern (SADP) within TEM. The effect of corrosive species on the local embrittlement of CMSX-4 is an area in which considerable further work should be focused on. Nevertheless, the effect of sea salt on the degradation of the scale under an applied stress highlights the importance of this testing approach as a method to study the failure mechanisms operating under the platform of turbine blades.

## Acknowledgements

We would like to thank James Willcocks and Aaron Hazell from Rolls-Royce for supporting this work in undertaking the XCT scanning of the specimens.

This work has been funded by Innovate UK ATI under the MALIT program (Grant no. 103081-263288)

## 7. References

- [1] Lortrakul P, Trice R W, Trumble K P, and Dayananda M A (2014) Investigation of the mechanisms of type-II hot corrosion of superalloy CMSX-4. *Corros. Sci.* 80: 408–415.
- [2] Oluwasegun K M, Ajide O O, Tanaka T, Zhang L, Ojo O A (2019) Hot corrosion performance of single-crystal CMSX-4 and CMSX-486 superalloys in the mixture of Na<sub>2</sub>SO<sub>4</sub>-NaCl melts. *J. Mater. Eng. Perform.* 28(9): 5509–5520.
- [3] Birks N, Meier G H, and Petit F S (2006) Hot corrosion. In: *Introduction to the high temperature oxidation of metals*, 2nd ed., New York: Cambridge University Press.
- [4] Luthra K L and Shores D A (1980) Mechanism of Na<sub>2</sub>SO<sub>4</sub> induced corrosion at 600°-900°C. *J. Electrochem. Soc.* 127(10): 2202–2210.
- [5] ISO - ISO 7539-5:1989 - Corrosion of metals and alloys — Stress corrosion testing — Part 5: preparation and use of C-ring specimens. [Online]. Available: <https://www.iso.org/standard/14318.html>. [Accessed: 06-Jan-2020].
- [6] ASTM, “G38-01(2013) - Standard practice for making and using C-ring stress-corrosion test specimens,” *ASTM Int.*, vol. 01.
- [7] Sumner J, Encinas-Oropesa A, Simms N J, and Nicholls J R (2014) Type II hot corrosion: Behavior of CMSX-4 and IN738LC as a function of corrosion environment. *Mater. Corros.* 65(2): 188–196.
- [8] Grabke H J, Reese E, and Spiegel M (1995) The effects of chlorides, hydrogen chloride, and sulfur dioxide in the oxidation of steels below deposits. *Corros. Sci.* 37(7): 1023–1043.
- [9] Spiegel M, Zahs A, and Grabke H J (2014) Fundamental aspects of chlorine induced corrosion in power plants. *Mater. High Temp.* 20(2): 153–159.
- [10] Zahs A, Spiegel M, and Grabke H J (2000) Chloridation and oxidation of iron, chromium, nickel and their alloys in chloridizing and oxidizing atmospheres at 400-700°C. *Corros. Sci.* 42(6): 1093–1122.
- [11] Montgomery M, Emanuel Maahn E, Gotthjælp K, Brøndsted P, Jansen P, and Markussen J (1997) High temperature corrosion in biomass incineration plants. p. 61.
- [12] Wang C J and Chang Y C (2002) TEM study of the internal oxidation of an Fe-Mn-Al-C alloy after hot corrosion. *Oxid. Met.* 57: 363-378.

- [13] Elliott P and Marsh G (1984) The oxidation of Incoloy 800 in moist air containing HCl(g) at 800°C. *Corros. Sci* 24(5).
- [14] O'Hagan C P, O'Brien B J, Leen S B, and Monaghan R F (2016) A microstructural investigation into the accelerated corrosion of P91 steel during biomass co-firing. *Corros. Sci.* 109: 101–114.
- [15] Nielsen H P, Frandsen F J, Dam-Johansen K, and Baxter L L (2000) Implications of chlorine-associated corrosion on the operation of biomass-fired boilers. *Prog. Energ. Comb. Sci.* 26(3): 283–298.
- [16] Chu H, Datta P K, and Straffordt K N (1995) Corrosion behavior of Fe(Ni)CrAlX alloys in an HCl-H<sub>2</sub>O-H<sub>2</sub> gas mixture at 800°C. *Oxid. Met.* 43: 491-508.
- [17] Hou P Y, Prüßner K, Fairbrother D H, Roberts J G, and Alexander K B (1998) Sulfur segregation to deposited Al<sub>2</sub>O<sub>3</sub> film/alloy interface at 1000°C. *Scr. Mater.* 40(2): 241–247.

2020-08-29

# Investigation into the effects of salt chemistry and SO<sub>2</sub> on the crack initiation of CMSX-4 in static loading conditions

Martinez, Fabian Duarte

Springer

---

Duarte Martinez F, Morar NI, Kothari M, et al., (2020) Investigation into the effects of salt chemistry and SO<sub>2</sub> on the crack initiation of CMSX-4 in static loading conditions. In: Superalloys 2020, Cham: Springer, pp. 753-762

10.1007/978-3-030-51834-9\_73

*Downloaded from Cranfield Library Services E-Repository*